Liu *et al.*
Chinese Journal of Mechanical Engineering (2023) 36:102
https://doi.org/10.1186/s10033-023-00920-7

Chinese Journal of Mechanical Engineering

ORIGINAL ARTICLE

Open Access

Cavitation Diagnostics Based on Self-Tuning VMD for Fluid Machinery with Low-SNR Conditions

Hao Liu[1], Zheming Tong[1*], Bingyang Shang[1] and Shuiguang Tong[1]

Abstract

Variational mode decomposition (VMD) is a suitable tool for processing cavitation-induced vibration signals and is greatly affected by two parameters: the decomposed number *K* and penalty factor *α* under strong noise interference. To solve this issue, this study proposed self-tuning VMD (SVMD) for cavitation diagnostics in fluid machinery, with a special focus on low signal-to-noise ratio conditions. A two-stage progressive refinement of the coarsely located target penalty factor for SVMD was conducted to narrow down the search space for accelerated decomposition. A hybrid optimized sparrow search algorithm (HOSSA) was developed for optimal *α* fine-tuning in a refined space based on fault-type-guided objective functions. Based on the submodes obtained using exclusive penalty factors in each iteration, the cavitation-related characteristic frequencies (CCFs) were extracted for diagnostics. The power spectrum correlation coefficient between the SVMD reconstruction and original signals was employed as a stop criterion to determine whether to stop further decomposition. The proposed SVMD overcomes the blindness of setting the mode number *K* in advance and the drawback of sharing penalty factors for all submodes in fixed-parameter and parameter-optimized VMDs. Comparisons with other existing methods in simulation signal decomposition and in-lab experimental data demonstrated the advantages of the proposed method in accurately extracting CCFs with lower computational cost. SVMD especially enhances the denoising capability of the VMD-based method.

Keywords Fluid machinery, Self-tuning VMD, Cavitation diagnostics, Hybrid optimized sparrow search algorithm

1 Introduction

Cavitation is one of the most dangerous failures in fluid machinery, in which vapor bubbles are generated inside impellers because of the partial pressure drop of the flowing fluid. Cavitation within fluid machinery can cause many undesirable effects, such as hydraulic performance degradation and impeller erosion. Diagnostics prior to the failure of unplanned breakdown has drawn substantial interest from researchers and engineers in the field of fluid engineering [1–3]. Various signals containing tremendous fault symptoms have been widely used for fluid machinery diagnostics by extracting cavitation-related characteristic frequencies (CCFs) [4–8]. Antoni [9], Li et al. [10], and Wang et al. [11] pointed out that a cyclostationary-based analysis of the rotating frequency (RF) and blade passing frequency (BPF) can help extract the components related to the modulation mechanism of flow-induced effects in pumps. Mousmoulis et al. [12] employed a spectral kurtosis (SK) tool for cavitation detection and found that the appearance of a BPF in the envelope spectrum is systematically related to cavitation development. Lee et al. [13] used the SK method to detect tip-vortex cavitation in a propeller. Han et al. [14] developed a technique for monitoring the cavitation inception speed based on the kurtosis of the detection of envelope modulation on noise (DEMON) spectrum. Chu et al. [15]

*Correspondence:
Zheming Tong
tzm@zju.edu.cn
[1] State Key Laboratory of Fluid Power and Mechatronic Systems, School of Mechanical Engineering, Zhejiang University, Hangzhou 310027, China

proposed an adaptive autogram approach based on the constant false alarm rate to extract cavitation features. Wu et al. [16, 17] proposed Enkurgram and a carrier wave extraction method for cavitation characterization. Tong et al. [2] proposed an early stage cavitation diagnosis approach that combines a vibration-signal-based neural network with high-speed photography. The above methods offer alternative solutions for predictive maintenance of pump cavitation.

The vibration response in fluid machinery is a superposition of multi-frequency characteristic information that contains various nonlinear and nonstationary components. Therefore, signal decomposition is a feasible option for dividing them into several subsignals to facilitate time-frequency analysis. Bao et al. [18] achieved adaptive and effective extraction of modulated cavitation noise from ship-radiated noise using the empirical mode decomposition (EMD) method. Azizi et al. [19] used EMD and the empirical wavelet transform (EWT) to extract cavitation features. Dai et al. [20] decomposed liquid-borne noise using complementary empirical EMD (CEEMD) to capture cavitation characteristics and sent the decomposition results into a deep residual shrinkage network for cavitation identification. Huang et al. [21] found that wavelet analysis is a more favorable and practical method for obtaining time-dependent frequency information for unsteady cavitating flows in mixed-flow pumps. However, these methods all have limitations. For instance, EMD is restricted by mode mixing and high noise sensitivity. Although noise-assisted techniques such as CEEMD mitigate mode mixing to some degree, the computational complexity increases dramatically, and added white Gaussian noise (WGN) cannot be effectively eliminated. The EWT essentially depends on the segmentation of the Fourier spectrum, and wavelet-based decomposition as a nonadaptive signal analysis method still requires wavelet basis functions in advance.

Variational mode decomposition (VMD), which is one of the latest signal decomposition techniques, was proposed by Dragomiretskiy and Zosso and has a strong theoretical basis [22]. According to the decomposition principle, the amplitude-modulation-frequency-modulation (AM-FM) components are extracted preferentially in the decomposition procedure of VMD [22, 23], which is also verified through our VMD decomposition test with a predefined mode number of 1 for the mixed signal from reference [24]. Cavitation-induced vibration signals perform broadband spectrum and rotation modulation, thus promoting VMD as a suitable tool to decompose the collected multicomponent signal into AM submodes, from which the characteristic frequencies can be extracted for diagnostics. Zhang et al. [25] successfully extracted the principal modes for fault diagnostics in the rolling bearing signal of a multistage centrifugal pump using VMD. Kumar et al. [26] used the symmetric single-valued neutrosophic cross-entropy of VMD for the identification of bearing defects in a centrifugal pump. Although better performance has been demonstrated in VMD with proper parameters than traditional decomposition methods [22, 27], both are hardly ever known a priori and may be selected unreasonably, thus promoting parameter-optimized-type VMD as a research topic. Search algorithms are introduced to determine the optimal pair of K and α, such as the genetic algorithm (GA) [28], grasshopper optimization algorithm (GOA) [29, 30], practical swarm optimization (PSO) [31], cuckoo search algorithm [32], and gray wolf optimization algorithm (GWO) [33]. With proper parameter optimization algorithms and optimization indexes, narrowband fault components can be extracted, and out-of-band noise can be effectively removed using the VMD method.

According to the literature review, although many efforts have been made in VMD-based fault diagnostics, some challenges still exist in current studies: Parameter-optimized VMDs generally face a heavy computational burden due to the many VMD trials in a broad optimization space. Using the same penalty factor to extract multi-bandwidth modes may cause unreasonable decomposition. Developing fault-information-guided decomposition combined with the latest proven optimization algorithm is necessary for vibration-based fault diagnostics in noisy environments.

Therefore, the contributions of this study are as follows:

(1) Proposing self-tuning VMD for cavitation diagnostics that replaces the joint optimization of parameters in traditional VMD with a progressive decomposition strategy.
(2) Developing a hybrid optimized sparrow search algorithm (HOSSA) and two fault-related indexes, envelope spectrum kurtosis (ESK) and kurtosis spectral entropy (KSE), for optimal penalty factor searching. Two preset criteria were designed to narrow the objective space for accelerated decomposition.

Benefiting from every optimal submode with personalized penalty parameters, self-tuning VMD (SVMD) greatly helps identify early stage defects that have weak fault features and are easily overwhelmed by heavy noise. The rest of the paper is organized as follows: In Section 2, the principles of VMD and the developed HOSSA are briefly introduced. The proposed method is described in Section 3. The numerical simulation and experimental validation are shown in Sections 4, 5, respectively. Finally, the conclusions are given in Section 6.

2 Brief Review of VMD and HOSSA

2.1 Theoretical Basis of VMD

VMD is a newly developed methodology for adaptive and quasi-orthogonal signal decomposition that can adaptively transform a real vibration signal f into K subcomponents u_k with specific sparsity properties and limited bandwidths in a nonrecursive manner. The bandwidth of each u_k is estimated through the H^1 Gaussian smoothness as a squared L^2-norm of the gradient, and its center frequency is denoted as ω_k. To minimize the sum of the spectral bandwidths of all subsignals, VMD is rewritten as a constrained variational problem in Eq. (1):

$$\begin{cases} \min\limits_{\{u_k,\omega_k\}} \left\{ \sum_K \left\| \partial_t \left[\left(\delta(t) + \frac{j}{\pi t} \right) \cdot u_k(t) \right] e^{-j\omega_k t} \right\|_2^2 \right\}, \\ \sum_{k=1}^K u_k = f, \end{cases} \tag{1}$$

where ∂_t is the partial derivative of the function at the time t, and $\delta(t)$ is the unit impulse function.

To solve the above variational problem, a quadratic penalty term α and Lagrangian multiplier $\lambda(t)$ are introduced, as described in Eq. (2):

$$\mathrm{L}(u_k, \omega_k, \lambda) = \alpha \sum_k \left\| \partial_t \left[\left(\delta(t) + \frac{j}{\pi t} \right) \times u_k(t) \right] e^{-j\omega_k t} \right\|_2^2 + \left\| f(t) - \sum_k u_k(t) \right\|_2^2 + \langle \lambda(t), f(t) - \sum_k u_k(t) \rangle. \tag{2}$$

The saddle point of the above augmented Lagrangian can be obtained using the alternating direction method of multipliers with alternating direction characteristics. The decomposed mode $\widehat{u_k}^1$ and its corresponding center frequency $\omega_k{}^1$, as well as the Lagrangian multiplier λ^1, are initialized first after pre-setting the decomposition mode number. Then, they are updated using Eqs. (3, 4, 5, 6):

$$\widehat{u_k}^{n+1}(\omega) \leftarrow \frac{\widehat{f}(\omega) \sum_{i<k} \widehat{u_i}^{n+1}(\omega) - \sum_{i>k} \widehat{u_i}^{n}(\omega) + \frac{\widehat{\lambda}^n(\omega)}{2}}{1 + 2\alpha \left(\omega - \omega_k^n \right)^2}, \tag{3}$$

$$\omega_k^{n+1} \leftarrow \frac{\int_0^\infty \omega \left| \widehat{u_k}^{n+1}(\omega) \right|^2 \mathrm{d}\omega}{\int_0^\infty \left| \widehat{u_k}^{n+1}(\omega) \right|^2 \mathrm{d}\omega}, \tag{4}$$

$$\widehat{\lambda}^{n+1}(\omega) \leftarrow \widehat{\lambda}^n(\omega) + \tau \left(\widehat{f}(\omega) - \sum_k \widehat{u_k}^{n+1}(\omega) \right), \tag{5}$$

$$\sum_k \frac{\left\| \widehat{u_k}^{n+1} - \widehat{u_k}^{n} \right\|_2^2}{\left\| \widehat{u_k}^{n} \right\|_2^2} < \varepsilon, \tag{6}$$

where $\widehat{u_k}^{n+1}(\omega)$, $\widehat{f}(\omega)$, and $\widehat{\lambda}^{n+1}(\omega)$ represent the corresponding Fourier transforms of u_k^{n+1}, f, and λ_k^{n+1}. u_k^{n+1} denotes the modal function at iteration $n+1$. When the loop is complete, the input signal will be decomposed into K modes. The general value of ε is 10^{-7}.

2.2 HOSSA Algorithm and Verification

SSA is a new swarm intelligence optimization algorithm inspired by sparrow foraging behavior and anti-predation behavior [34]. Here, HOSSA was developed based on the original SSA by adopting two perturbation strategies incorporated with chaos initialization. The input parameters were initialized referring to the sparrows' population (pop), producers (PN), scroungers ($pop - PN$), and scouters (SN), and the maximum iterations ($T_{\max}$); upper bound (ub), and lower bound (lb) of the search in d-dimensional space. The initial location of sparrows was defined as $X_{i,j} = \left[X_{1,1} X_{1,2} \cdots X_{pop,D} \right], i = 1, 2, \cdots, pop, j = 1, 2, \cdots, D$. Improved tent chaotic mapping was adopted to further enhance the diversity of the sparrow population. The tent chaotic sequence is given by

$$z_{i+1,j} = \begin{cases} 2z_{i,j} + \frac{rand(0,1)}{pop}, 0 \le z_i \le 0.5, \\ 2(1 - z_{i,j}), + \frac{rand(0,1)}{pop}, 0.5 < z_i \le 1, \end{cases} \tag{7}$$

where i indicates the number of current mappings, and z_i and z_{i+1} are the mapping values in the current and subsequent states, respectively.

The expression after the Bernoulli transformation is

$$z_{i+1,j} = \left(2z_{i,j} \right) mod 1 + \frac{rand(0,1)}{pop}. \tag{8}$$

The ranges of the chaos variables were transferred into the optimization variables to achieve sparrow population initialization.

$$X_{i,j}^0 = z_{i,j}(ub - lb) + lb, \tag{9}$$

where $X_{i,j}^0$ represents the ith individual sparrow in the jth dimension after initialization, and lb and ub are the lower and upper bounds of the mth dimension, respectively.

The locations of producers can be updated using Eq. (10):

$$X_{i,j}^{t+1} = \begin{cases} X_{i,j}^{t} \cdot \exp\left(-\frac{i}{\sigma \cdot T_{\max}}\right), R_2 < ST, \\ X_{i,j}^{t} + Q \cdot \boldsymbol{L}, R_2 \geq ST, \end{cases} \tag{10}$$

where t represents the current iteration, $\sigma \in (0, 1]$ is a random value, Q represents a random number that follows a normal distribution, $\boldsymbol{L}$ denotes a $1 \times d$ matrix all filled by element 1, and $R_2 \in [0, 1]$ and $ST \in [0.5, 1]$ are the warning value and safety threshold, respectively. $R_2 < ST$ means that producers are able to continue an extensive search with no predators around, while $R_2 \geq ST$ means that sparrows have been exposed to the predator, and all sparrows need move to other safe areas.

The locations of scroungers can be updated using Eq. (11):

$$X_{i,j}^{t+1} = \begin{cases} Q \cdot \exp\left(-\frac{X_{\text{worst}} - X_{i,j}^{t}}{\sigma \cdot T_{\max}}\right), i > pop/2, \\ X_{p}^{t+1} + \left|X_{i,j}^{t} - X_{p}^{t+1}\right| \cdot A^{+} \cdot L, i \leq pop/2, \end{cases} \tag{11}$$

where X_p and X_{worst} represent the current optimal and worst positions, respectively. $\boldsymbol{A}$ contains d elements with 1 or -1, $\boldsymbol{A}^{+} = \boldsymbol{A}^{\mathbf{T}}(\boldsymbol{A}\boldsymbol{A}^{\mathbf{T}})^{-1}$, and $i > pop/2$ indicates that scrounger i tends to starve and must fly to a new position.

The hazard perceivers account for 20% of the entire population, and they renew locations according to Eq. (12):

$$X_{i,j}^{t+1} = \begin{cases} X_{\text{best}}^{t} + \beta \cdot \left|X_{i,j}^{t} - X_{\text{best}}^{t}\right|, f_i > f_g, \\ X_{i,j}^{t} + \kappa \cdot \left(\frac{\left|X_{i,j}^{t} - X_{\text{worst}}^{t}\right|}{(f_i - f_w) + \varepsilon}\right), f_i = f_g, \end{cases} \tag{12}$$

where X_{best}^{t} represents the best position in the current search space, β is the step adjustment factor, which obeys a standard normal distribution, f_i, f_g, and f_w denote the fitness value of the sparrow i, global optimal fitness value, and global worst fitness value, respectively, $\kappa \in [-1, 1]$ controls the movement direction of the current sparrow, ε is introduced to prevent the denominator from appearing to be zero, $f_i > f_g$ indicates that sparrow i is located at the edge of the population where it is more vulnerable to predators, $f_i = f_g$ means that sparrow i in the center of the population needs to approach the surroundings for anti-predation.

After one update operation, the greedy strategy was introduced to determine which disturbance strategy to adopt by comparing the fitness values of each individual f_i and the entire population f_{avg} and to decide whether to replace the original individual according to the new and old locations.

$$X_{\text{best}}^{t+1} = \begin{cases} X_{\text{best,mu}}^{t+1}, f_i < f_{\text{avg}} \text{ and } f_{\text{new}} > f_i, \\ X_{\text{best,tcp}}^{t+1}, f_i \geq f_{\text{avg}} \text{ and } f_{\text{new}} > f_i, \\ X_{\text{best}}^{t}, \text{otherwise}, \end{cases} \tag{13}$$

where f_i and f_{new} represent the fitness before and after the update operation, respectively, and $X_{\text{best,tcp}}^{t+1}$ is the small tent chaos disturbance added to the current optimization solution using Eq. (14):

$$X_{\text{best,tcp}}^{t+1} = (X_{\text{best}}^{t} + X_{i,j})/2, \tag{14}$$

where $X_{\text{best,mu}}^{t+1}$ is the hybrid mutation operator with Gaussian and Cauchy, as defined in Eq. (15):

$$\begin{aligned} X_{\text{best,mu}}^{t+1} = X_{\text{best}}^{t} + \big(&\lambda_1 \cdot Cauchy(0, 1) \\ &+ \lambda_2 \cdot Gaussian(0, 1)\big) \oplus X_{\text{best}}^{t}, \end{aligned} \tag{15}$$

$$\lambda_1 = 1 - \frac{t^2}{T_{\max}^2}, \lambda_2 = \frac{t^2}{T_{\max}^2}, \tag{16}$$

where X_{mu}^{t} is the individual with a mutation at iteration t, Cauchy (0,1) and Gaussian (0,1) are both random variables that follow Cauchy and Gaussian distributions with a mean of 0 and a variance of 1, and λ_1 and λ_2 both adjust the mixture of Cauchy and Gaussian mutation. A higher λ_1 expands the search scope at the beginning of the iterations, whereas a higher λ_2 accelerates the convergence process during later iterations.

The performance verification of HOSSA is shown in Figure 1.

The generalized Rosenbrock function (Eq. (17)) was applied to investigate the efficiency of HOSSA, as shown in Figure 1(a), where the color bar represents the function value. Several state-of-the-art algorithms such as GWO, PSO, the whale optimization algorithm (WOA), ant lion optimizer (ALO), moth-flame optimization (MFO), multi-verse optimizer (MVO), and SSA were selected for comparison. The parameter settings for each algorithm are shown in Table 1. The run was conducted on a computer with an AMD Ryzen 7 1700X CPU and 32 GB of RAM using the MATLAB R2021a platform. The best value, average value, standard deviation (Std) of the objective function values, and computing time were used to evaluate convergence results:

$$f(x) = \sum_{i=1}^{d} \left[100 \times (x_{i+1} - x_i)^2 + (x_i - 1)^2\right]. \tag{17}$$

Figure 1(b) and Table 2 both indicate that GWO, PSO, the WOA, and MFO presented highly similar convergence behaviors, with the fastest speed compared to the

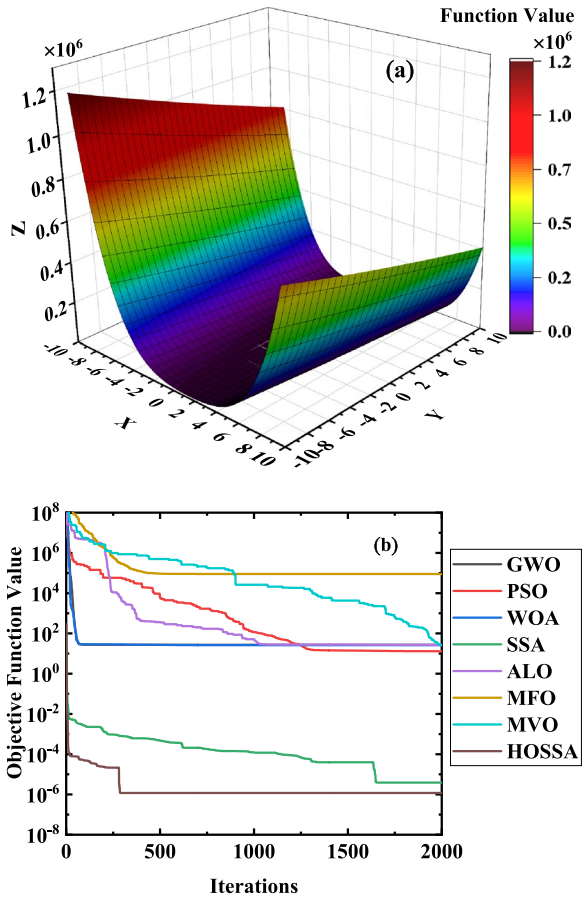

Figure 1 Performance verification of HOSSA: **a** Rosenbrock function, **b** Convergence curves of eight algorithms

other competitive algorithms. ALO, MFO, and MVO performed worst in terms of accuracy, reliability, and consistency, with the highest Std and average fitness values. In sharp contrast to the other six algorithms, the SSA and HOSSA had the minimum values of average optimization results and Std, which consequently indicates the highest accuracy, stability, and robustness through different runs. As for the average time over 30 runs, although the SSA was not the most time-saving one at 1.24 s, the small disadvantage of optimization time could be ignored due to its significant superiority in other evaluation indicators. HOSSA outperformed the SSA in terms of the search capability and computational complexity. Therefore, HOSSA appears to be more suitable than the other algorithms, including the original SSA, in searching for the optimal α.

3 Proposed SVMD Method

This section introduces the proposed SVMD signal decomposition framework. The main strategy is to first narrow the search space based on the thresholds relative to the reference mode and then search the extremum using the proposed HOSSA based on the constructed objective function. Thus, these two aspects are introduced prior to the proposed method, the procedure for which is illustrated later.

3.1 Optimization Objective Function

The selection of optimal α depends on the optimization objective function. Considering that the collected signal in fluid machinery presents a prominent amplitude modulation phenomenon, this study introduces two indexes, ESK and KSE, which consider both the impulsive and periodic behaviors of the fault impulses simultaneously.

$$kurt_f = \frac{\mathrm{E}\left[f(t) - u_f\right]^4}{{\sigma_f}^4}, \tag{18}$$

where $kurt_f$ is the kurtosis of signal $f(t)$, u_f and σ are the mean and standard deviation, respectively, and $\mathrm{E}[\cdot]$ is the operator that computes the expectation of a series.

The envelope spectrum $ES(\omega)$ of $f(t)$ is obtained using Hilbert demodulation and a fast Fourier transform (FFT), and the ESK is given in Eq. (19) [35–38]:

$$ESK = \frac{\mathrm{E}\left[ES(\omega) - u_{ES(\omega)}\right]^4}{{\sigma_{ES(\omega)}}^4}. \tag{19}$$

Table 1 Parameter settings of involved algorithms

Algorithm	Parameter settings
GWO	Convergence constant a decreases linearly from 2 to 0; r_1 =0–1, r_2=0–1
PSO	Acceleration constants are both set as 2, inertia weights are set as ($\omega_{\min} = 0.2, \omega_{\max} = 0.9$)
WOA	Convergence constant a decreases linearly from 2 to 0; $\boldsymbol{\alpha}_2$ decreases from − 1 to − 2; r_1 =0–1, r_2=0–1
SSA	The number of producers is 20%. The number of dangers is 10%. The safety threshold is set as 0.8
ALO	The number of populations and iterations
MFO	The number of populations and iterations
MVO	Minimum and maximum of wormhole existence probability of 0.2 and 1, respectively

Table 2 Comparisons of HOSSA and other competitors

Algorithm	Best	Average	Std	Average time over 30 runs (s)
GWO	24.80	26.92	0.81	0.59
PSO	7.56	53.09	37.31	0.32
WOA	25.83	26.48	0.68	0.51
SSA	9.13×10^{-9}	3.2×10^{-6}	4.24×10^{-6}	1.24
ALO	22.06	164.65	314.46	115.08
MFO	0.52	6471.66	22358.94	0.56
MVO	26.20	322.59	650.31	0.89
HOSSA	2.9×10^{-6}	4.3×10^{-6}	5.1×10^{-6}	0.82

Kurtosis represents the impact characteristics of signals, envelope spectral entropy represents the periodic characteristics of signals, and a new index, KSE, can be expressed as follows:

$$ESE = -\sum_{i=1}^{N} p_i \ln p_i, \tag{20}$$

$$KSE = \frac{kurt_f}{ESE}, \tag{21}$$

where ESE is the envelope spectral entropy, and P_i is the envelope spectrum that is processed into a probability distribution sequence.

Figure 2 shows the formation of cavitation-induced vibration signals in fluid machinery. Previous studies have observed evident AM phenomena, indicating that the amplitude of the collected signal changes periodically with a moving impeller. Using ESK to emphasize the dominant peak-like demodulated RF, the BPF and its harmonics are helpful in identifying multiple cavitation-induced impacts, which present a discrete wideband frequency distribution like the filtered heavy WGN with a kurtosis smaller than 3 [16]. However, a high KSE trend indicates that the submode is more likely to be periodically impulsive. The selection of the optimization functions is guided by Eq. (22):

$$fit = \begin{cases} -\underset{(1,\alpha)}{\operatorname{argmin}}\{KSE(u_k)\}, kurt_{u_k} \geq 3, \\ -\underset{(1,\alpha)}{\operatorname{argmin}}\{ESK(u_k)\}, kurt_{u_k} < 3. \end{cases} \tag{22}$$

3.2 Stop Criterion

In this study, the power spectrum difference tracking method was adopted to adaptively decide whether to continue with the next iteration. The power spectrum was calculated using Eq. (23):

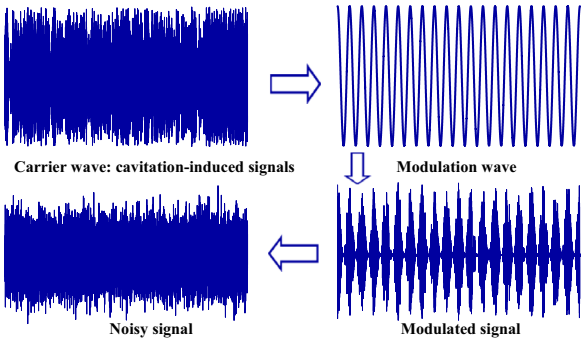

Figure 2 Format of cavitation-induced vibration signals in fluid machinery

$$PS(\omega) = \left|FFT(f(t))\right|^2. \tag{23}$$

After obtaining K submodes of $u_k(t)$, the signal was reconstructed using Eq. (24):

$$f' = \sum_{i=1}^{K} u_k(t). \tag{24}$$

The similarity between the reconstructed signal and initial signal was characterized based on the correlation coefficient of their power spectra, as calculated by Eq. (25):

$$c_{PS_f PS_{f'}} = \frac{\sum_{i=1}^{n}\left(PS_f - \overline{PS_f}\right)\left(PS_{f'} - \overline{PS_{f'}}\right)}{\sqrt{\sum_{i=1}^{n}\left(PS_f - \overline{PS_f}\right)^2}\sqrt{\sum_{i=1}^{n}\left(PS_{f'} - \overline{PS_{f'}}\right)^2}}. \tag{25}$$

The power spectrum of the residual signal could be ignored after extracting the dominant fault-related signal due to its low contribution to further improving $c_{PS_f PS_{f'}}$. The experience demonstrated that the stopping decomposition when $c_{PS_f PS_{f'}}$ is greater than 0.9 involves a significant trade-off between decomposition speed and reconstruction accuracy.

3.3 Procedure of SVMD

Based on prior knowledge, this study proposed SVMD for fault diagnostics. A rough-to-precise strategy of searching for optimal α was explored based on the proposed reference mode and developed HOSSA algorithm. A flowchart of this is displayed in Figure 3. The details are summarized as follows:

Step 1 Set the raw vibration signal as a residual signal and perform VMD operation on the residual signal.

Step 2 Select eight α markers from initial optimization space [200, 20000], detailed as 200, 600, 2000, 3000, 6000, 10000, 15000, and 20000. Run VMD with parameter

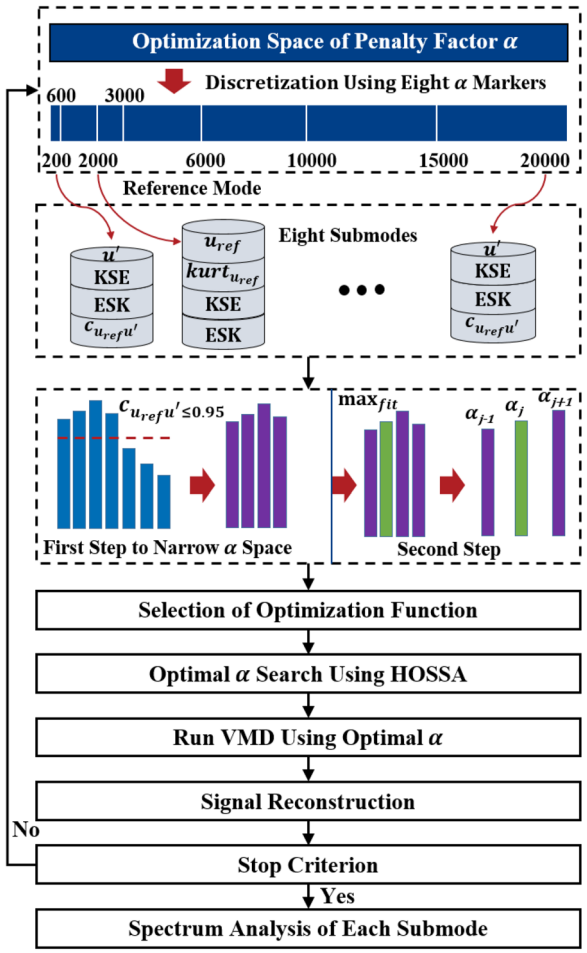

Figure 3 Flowchart of the proposed SVMD

Step 4 Determine the objective function guided by the signal type. Choose min(*KSE*) as the objective function when $kurt_{u_{ref}} \geq 3$; Otherwise, select min(*ESK*).

Step 5 Find the largest fitness selected in Step 4 and choose its corresponding α marker as the center of the new parameter ranges of the optimal α. For example, if α=[2000, 3000, 6000, 10000, 15000, 20000] is proven valid after Step 3 and α=6000 corresponds to the largest ESK, then the new optimization space becomes 3000–10000 instead of the original range of 2000–20000. If α=20000 corresponds to the largest ESK, the new optimization space becomes 15000–20000.

Step 6 Apply HOSSA to search for the optimal α in the final optimization space, which has been narrowed after Step 3 and Step 5.

Step 7 Run VMD using the optimal α and K=1 to obtain the single-decomposition mode.

Step 8 Reconstruct the signal using Eq. (24) until satisfying $c_{PS_f PS_{f'}} > 0.9$. Otherwise, let $f(t) = f(t) - f'(t)$ and return to Step 1, and continue with the next SVMD.

4 Validation of Proposed Method

4.1 Vibration Model

Numerical simulation of the cavitation-induced vibration model was configured using Eq. (26), the waveforms of which are shown in Figure 4(a)–(d). To verify the validity of SVMD, the decomposed performance of the simulation signals was investigated under different noise interference conditions. CEEMD, fast Kurtogram, and original VMD with different parameters were also used for comparison.

$$\begin{cases} x_1(t) = 0.3\cos\left(2\pi f_1 t\right), \\ x_2(t) = 0.45\cos\left(\pi t^2 + 2\pi t\right)\sin\left(2\pi f_2 t\right), \\ c_1(t) = \sum_i 2\pi A e^{-0.04\pi f_{c1}\ (t-iT_i)}\cos\left(\sqrt{1-0.02^2} f_{c1}(t-iT_i)\right), \\ c_2(t) = \sum_j 3\pi e^{-0.07\pi f_{c2}\ (t-jT_i)}\cos\left(\sqrt{1-0.035^2} f_{c2}(t-jT_i)\right), \\ n(t) = \eta, \\ x(t) = x_1(t) + x_2(t) + c_1(t) + c_2(t) + n(t), \end{cases} \tag{26}$$

settings of K=1 and the above α markers to get a total of eight submodes termed u', of which the submode under α=2000 is regarded as a reference mode u_{ref}. Calculate the kurtosis $kurt_{u_{ref}}$, ESK, and KSE of the other seven u', and their correlation coefficients of $c_{u_{ref}\ u'}$ with u_{ref}.

Step 3 Narrow the search space of optimal α by eliminating invalid α markers when satisfying $c_{u_{ref}\ u'} \leq 0.95$.

where $x_1(t)$ denotes a harmonic signal, f_1 is the shaft frequency at 25 Hz, $x_2(t)$ represents a multicomponent modulation signal with a variable frequency, f_2 equals to 200 Hz, $c_1(t)$ is used to simulate the impulses induced by the bubble collapse near the pump body, f_{c1} is the resonance frequency at 3000 Hz, A was set as a random value between zero and two in this study, T_i is the time interval of 0.00125 between two adjacent impacts. $c_2(t)$ stands for the periodic transient impulses that may be caused by a fault in the shaft and bearing system, and $n(t)$ is the additive WGN. The sampling frequency and number of

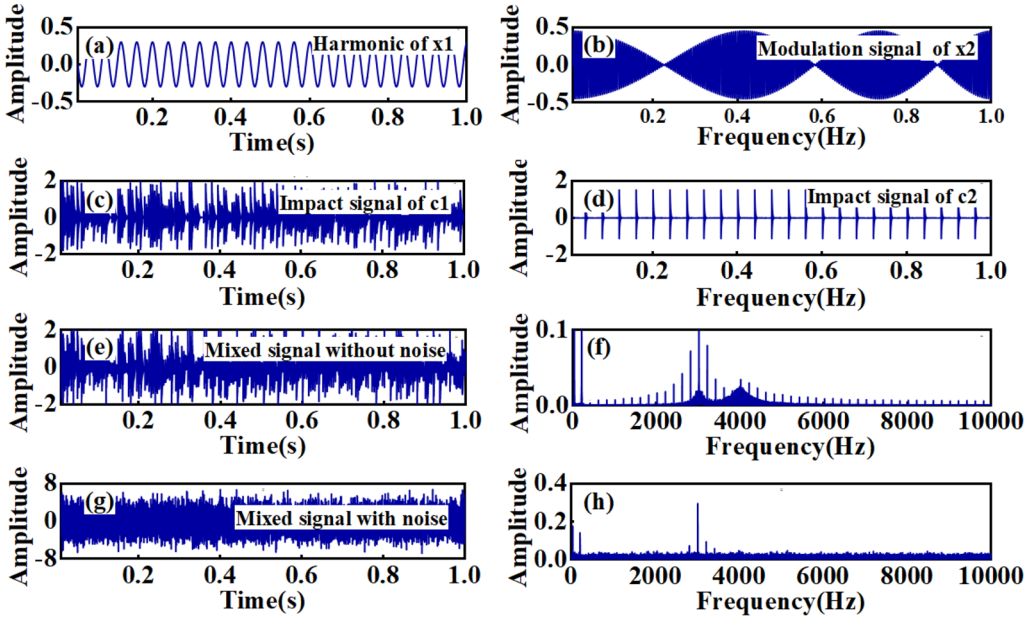

Figure 4 Time series of the simulated signals

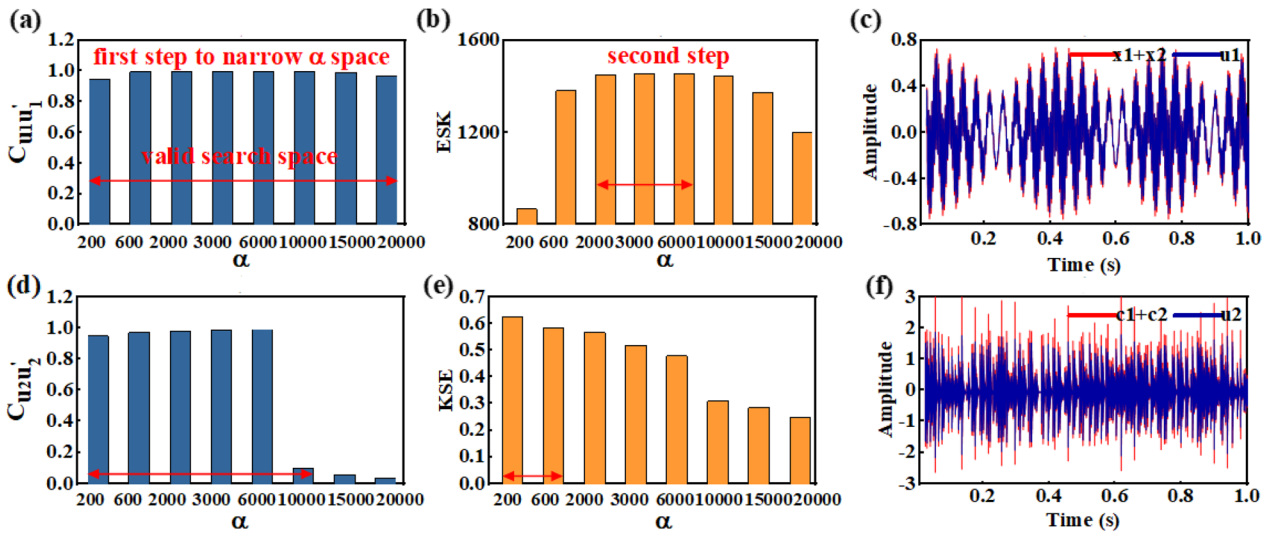

Figure 5 Two SVMD operations and their decomposition results

signals were set to 20 kHz and 1 s, respectively. Different signal-to-noise ratios (SNRs) were created by adding WGN to the simulated signal to discuss the impact of smearing the impulsive signature.

4.2 Decomposition of Noise-Free Signals

Figure 5 shows the decomposition process of the noise-free signal using SVMD. The range covered by the red arrow represents the valid optimization space. Figure 5(a), (b) indicate that SVMD can provide an optimal α of 4192 for the first decomposed mode u_1, which was found using HOSSA based on the objective function fit_{ESK} within the refined α range of 2000–6000. Adopting the maximum correlation coefficient between u_1 and $x_1(t) + x_2(t)$ as the objective function resulted in the optimal penalty factor of 5420. The second SVMD operation was performed after peeling u_1 off, as shown in Figure 5(d), (e). The optimal penalty factor of u_2 was found to be 200. Coincidentally, the

penalty factor corresponding to the maximum correlation coefficient between the second decomposed mode u_2 and impact components $c_1(t) + c_2(t)$ was also 200. This proves the validity of our proposed index in effectively finding the optimal decomposition parameters. After peeling twice, a larger $c_{PS_fPS_{f'}}$ of 0.998 was used to stop further decomposition. Figure 5(c), (f) present the decomposition results of the noise-free signal using the SVMD approach with final optimal penalty factors of 4192 and 200, respectively, from which meaningful signals with the same features were centralized in one mode. Although the amplitude of the decomposed modes was slightly attenuated compared to the original components, a high correlation coefficient verified the excellent decomposition ability of the proposed method.

In contrast, HOSSA-VMD was performed on the same the signal as the objective function of the average KSE of all modes directly, through which the optimal mode number and penalty factor were determined to be 2 and 349, respectively. Compared to fixed-parameter VMD, whose optimal parameter pair highly depends on empirical choices, HOSSA-VMD achieved adaptive decomposition and satisfactory decomposition results, as shown in Figure 6.

Figure 7 shows the six IMFs of CEEMD. These results exhibited obvious mode aliasing. The impact components suffered from distortions and were decomposed into the first three modes; in particular, the first mode retained the majority of the original signal. The harmonic

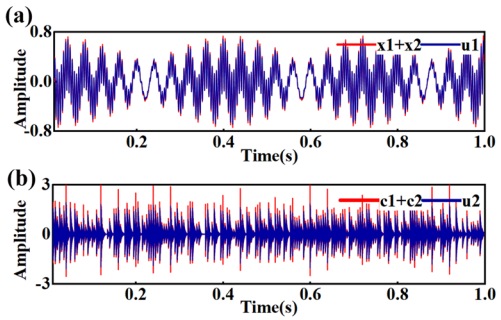

Figure 6 HOSSA-VMD decomposition with $K = 2$, $\alpha = 349$

signal was decomposed into the last three modes as residual components. This produced an obviously poorer decomposition effect than SVMD and HOSSA-VMD in the processing of multicomponent signals.

Figure 8 shows the Kurtogram of the simulated data, where the color bar represents the kurtosis value for a range of window lengths and frequencies. A kurtosis dominant frequency band with a center of 8333 Hz (f_c) and a bandwidth of 3333 Hz (B_w) stood out from the array of frequency bands. However, it failed to locate the preset resonance band of the simulated signal and identify the impact signals whose frequencies were concentrated around 3000 Hz and 4000 Hz.

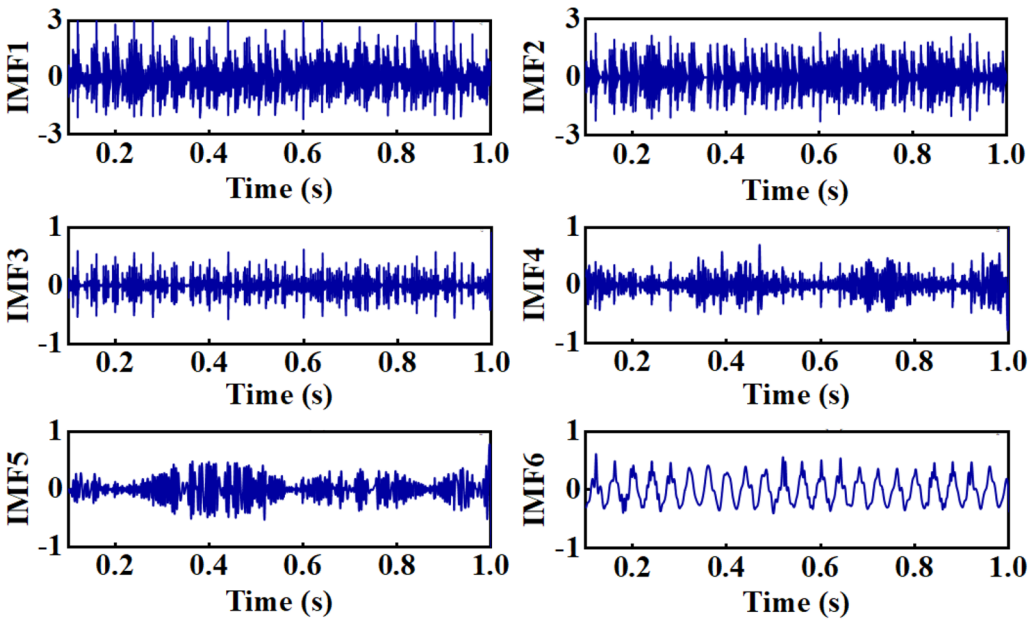

Figure 7 Six IMFs from the CEEMD method

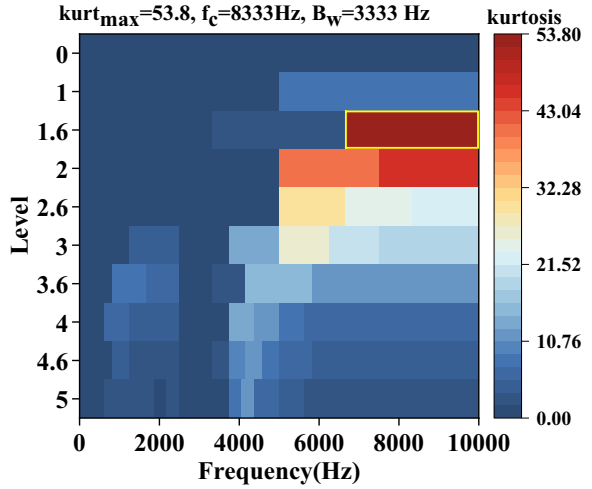

Figure 8 Kurtogram of the original signal

4.3 Comparison under Different SNRs

To quantify the decomposition ability of the five methods under different noise levels, the contrastive indicator correlation coefficients between the original and reconstructed signals were calculated, as shown in Table 3. $c_{u_1(x_1+x_2)}$ is the maximum correlation coefficient between the first decomposed mode and the original signal of $x_1(t)+x_2(t)$, $c_{u_2(c_1+c_2)}$ is the maximum correlation coefficient between the second decomposed mode and the original signal of $c_1(t)+c_2(t)$. OVMD refers to an optimal VMD-based method that adopts the largest correlation coefficient between the decomposed submodes and subcomponents of the original signal as the objective function. Consequently, they were all close to 1 under the no-noise condition, except for the failure of the SK method. The decomposition ability of all the methods became weaker as the SNR decreased. Clearly, SVMD retained satisfactory applicability for processing composite signals with different components compared to the SSA-VMD, CEEMD, and SK methods, even in a noisy environment. The proposed SVMD scheme almost achieved optimal decomposition theoretically through the OVMD method in the four SNR cases. However, it is impossible to use OVMD in practice because the signal components are unknown in advance. Fortunately, SVMD can intelligently determine a parameter pair without any prior knowledge of the signal to be decomposed.

To evaluate the efficiency of the involved approaches, the computational expenses are also reported in Table 3. VMD was performed on the signal in Eq. (26) with varying mode numbers. It was found that the decomposition time of the VMD-based methods significantly increased with increasing decomposition modes and decreasing SNR. The comparison showed that SSA-VMD and OVMD were the most time-consuming methods, with the only difference being in the optimization objective function. Twenty sparrow populations were assigned to directly search for the optimal *K*-α pair in a huge optimization space with K=[2, 9] and α=[100, 9000], and multiple VMD operations were performed in 10 iterations, which was responsible for the heavy computational burden. Benefiting from the reduced optimization space and faster convergence speed of HOSSA itself, SVMD provided 4.7–14.2 times higher decomposition efficiency than other parameter-optimized VMDs. Although the CEEMD and SK methods provided the highest decomposition efficiencies, they were not sufficiently competitive under the premise of prioritizing decomposition accuracy.

Table 3 Comparison of methods on decomposition accuracy and efficiency

Signal	Method	$c_{u_1(x_1+x_2)}$(%)	$c_{u_2(c_1+c_2)}$(%)	Time (s)
f without noise	SVMD	99.89	98.54	1166
	SSA-VMD	99.74	97.42	13123
	CEEMD	92.96	93.74	3.4
	OVMD	99.89	98.54	16580
	SK	0.02	21.29	2.4
f with noise SNR=0 dB	SVMD	94.51	88.12	3326
	SSA-VMD	93.92	82.16	15682
	CEEMD	62.82	63. 1	3.2
	OVMD	94.51	88.59	15965
	SK	0	18.05	2.9
f with noise SNR=−5 dB	SVMD	84	79.9	4582
	SSA-VMD	82.41	65.47	25246
	CEEMD	48.93	42.31	4.1
	OVMD	84.06	81.07	21584
	SK	0	12.3	3.4
f with noise SNR=−10 dB	SVMD	63.14	72.02	5020
	SSA-VMD	57.76	45.84	30036
	CEEMD	29.52	27.19	5.5
	OVMD	63.15	72.03	24364
	SK	60.95	0	3.6

In summary, the above simulation fully highlights the advantages of SVMD's anti-aliasing characteristics and the noise robustness of the proposed method for processing multicomponent nonstationary signals.

5 Cavitation Diagnostics in Fluid Machinery

5.1 Cavitation Experiment

Cavitation is a common problem encountered in fluid machinery. In this study, an in-lab pump system was selected to demonstrate cavitation diagnostics. The cavitation experiments were conducted on a closed test bench, as shown in Figure 9, in which the test pump and measuring devices were arranged in the pipeline. A liquid-ring

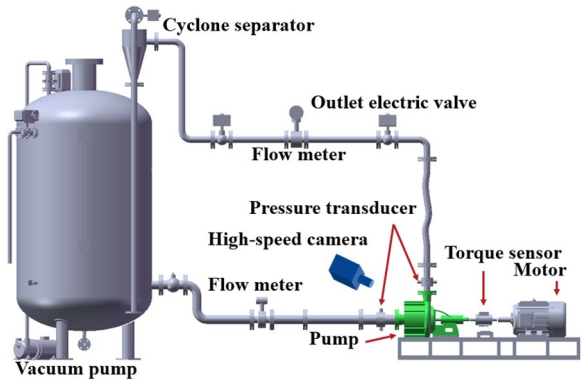

Figure 9 Test bench and instrumentation

vacuum pump was used to promote cavitation development by gradually reducing the pressure of the pump inlet. To avoid the temperature and dissolved air effects on the onset of cavitation, we designed a low-pressure degassing tank with a cyclone separator to exhaust the dissolved air in the water as much as possible and stop the pump after a period of time to cool the water. A test pump with seven blades was driven at a constant rotational speed and flow rate. For each cavitation condition, vibration measurements were conducted synchronously using PCB353-type sensors via an NI data acquisition board (NIUSB-6212BNC) and recorded on a laptop using LABVIEW software with a 25600-sample frequency. To ensure the interpretability of the vibration signals and net positive suction head available (NPSHa) as much as possible, high-speed camera measurements were additionally supplied, which can provide details of the cavitation flow structure in the pumps.

5.2 Cavitation Performance

Figure 10(a) shows the cavitation performance curve of the tested pump obtained at $1.2Q_d$ and 1500 r/min. The 3% head-drop point is also marked. To further define the cavitation states, a correlation between the characteristic curve and cavitation structure was built, and a total of six operating points along with the curve were selected to represent the entire cavitation process (represented by black dots in Figure 10(a)). According to the visualization results recorded using high-speed photography in Figure 10(b), inception cavitation occurred at NPSHa=3.77 m. The pump head sharply decreased when NPSHa was below 2.95 m, and the cavitation was severe before the critical cavitation point. Cavitation bubbles within the impeller mainly existed in the form of attached cavities on the blades, such as the sheet cavity at the leading edge of the blade and the cloud cavity occupying the majority of the blade surfaces.

5.3 Extracting Characteristic Frequency

A serious cavitation state cav_{15} was selected as the demonstration case. Figure 11 shows the frequency and envelope spectra of the submodes decomposed using the SVMD and fixed-parameter VMD methods. The BPF was clearly visible in the envelope spectrum of each submode, but its 2-octave frequency mainly appeared in

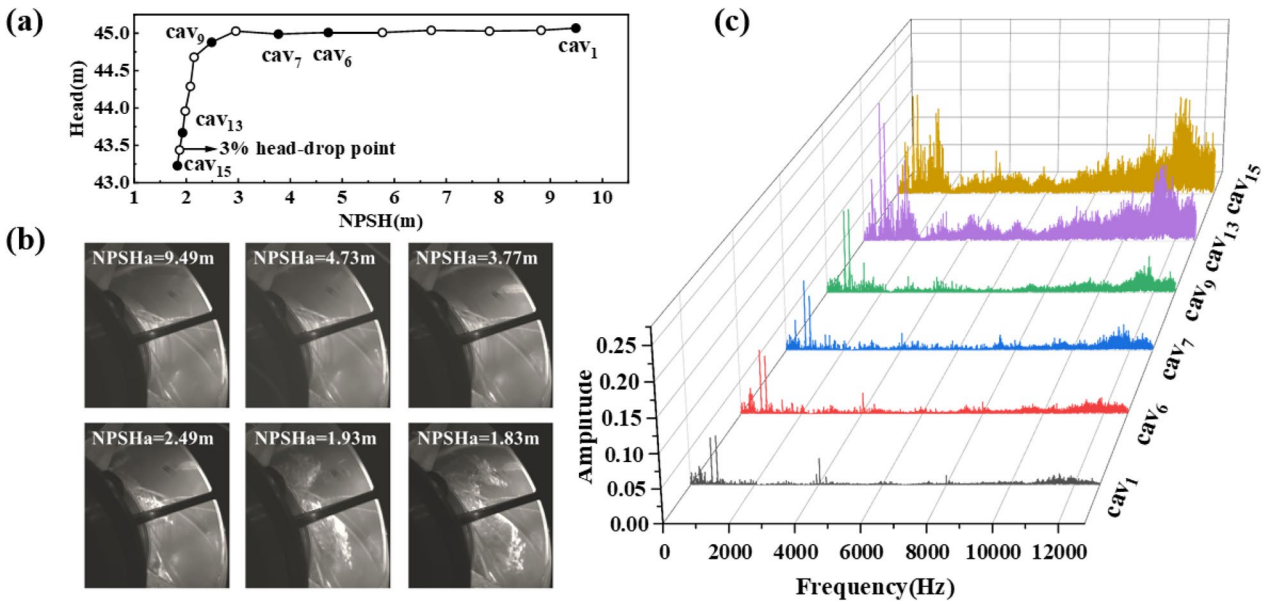

Figure 10 Cavitation test results: **a** Cavitation performance of the test pump operated at 1500 r/min and $1.2Q_d$, **b** Evolution of cavitation in the pump impeller with different NPSHa, **c** Frequency spectrum under six cavitation states

the high-frequency submodes in u6 of SVMD and u5 of VMD. Both SVMD and VMD can realize the extraction of CCFs from raw signals without noise interference and are suitable for use in quiet environments, such as building water supply pumps.

Under complex service scenarios containing multi-component linkages and uncontrolled human activities, such as power stations and ships, the cavitation-induced vibration signature is usually polluted by strong background noise. Figure 12 shows the cavitation diagnosis under such low-SNR conditions. Two indicators of kurtosis and EK of each submode decomposed by SVMD and VMD for − 10 dB and − 20 dB were compared. EK refers to the product of kurtosis and the energy ratio of the submode to the total energy. The meaningful submodes are presented in Figure 13. After adding WGN to reach a SNR of − 10 dB, obvious spectral peaks at the BPF and its second harmonics could only be found in the envelope spectrum of modes u5 and u6. When increasing WGN until the SNR reached − 10 dB, the characteristic frequency BPF and its multiplication were still prominent in mode u8 obtained by SVMD, in contrast with the buried peak of the envelope spectrum in all submodes using VMD. Obviously, SVMD achieved improvements based on VMD methods. To further verify the performance of SVMD, we compared it with the Kurtogram [12–14], Autogram [15], and IESCFFOgram [39], which have been successfully demonstrated for fault diagnosis of rotating machinery. Figure 14 shows the demodulation results of pump cavitation-induced signals (cav_{15}) under −20 dB SNR conditions. The color bars in Figure 14(a), (d) represent the kurtosis values, and that in Figure 14(g) represents the energy ratio (ER) of all CFFs to the improved envelope spectrum. From their provided demodulation bands, none of the CCFs could be found after the envelope spectrum analysis, which indicates that they lost the capability to identify the characteristic frequency bands of the cavitation-related signals in noisy environments. In contrast, submode u6 obtained by SVMD contained a meaningful eigenfrequency of the BPF.

Although SVMD and VMD can both properly and effectively extract the characteristic frequencies occurring in fluid machinery under high SNR levels, the proposed method can obtain higher values of kurtosis and EK, which guarantees the ability of SVMD to maintain cavitation diagnosis under a low SNR. The EK index comprehensively considers the spectral and energy dominance. The submode corresponding to the highest EK

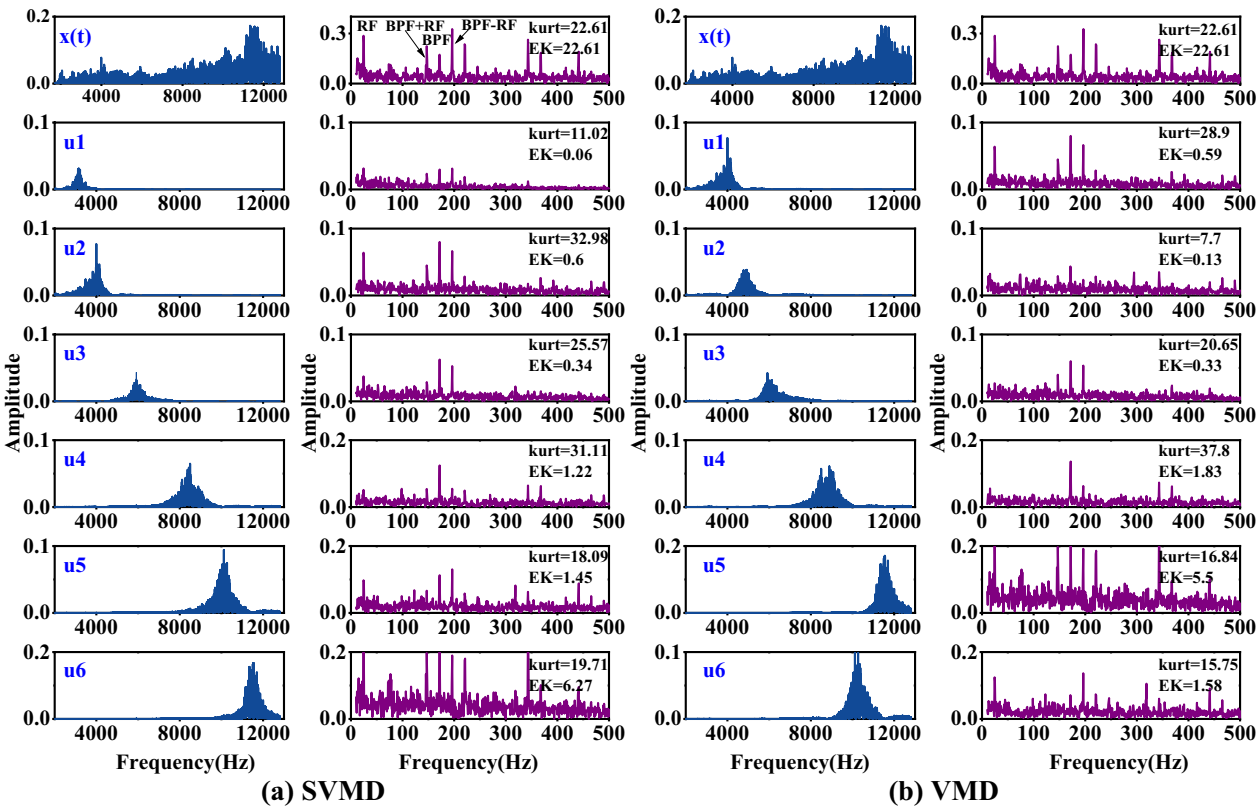

Figure 11 Frequency and envelope spectra of cav_{15} without noise using SVMD in **a**, and VMD with K=6, α = 2000 in **b**

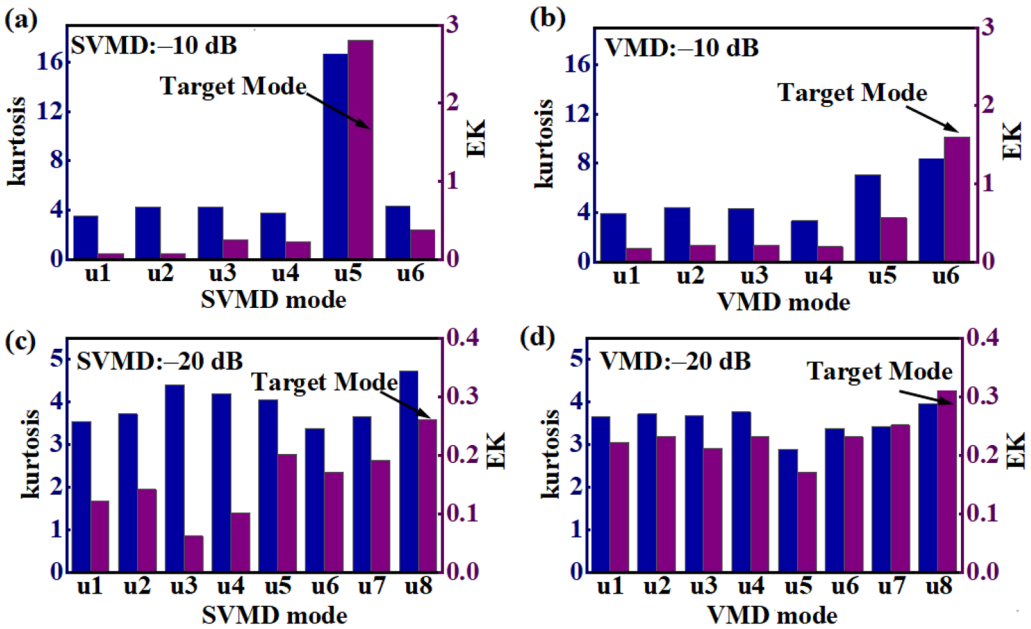

Figure 12 Two indicators of kurtosis and EK of each submode decomposed by SVMD in **a** and **c** and VMD in **b** and **d** for – 10 dB and – 20 dB

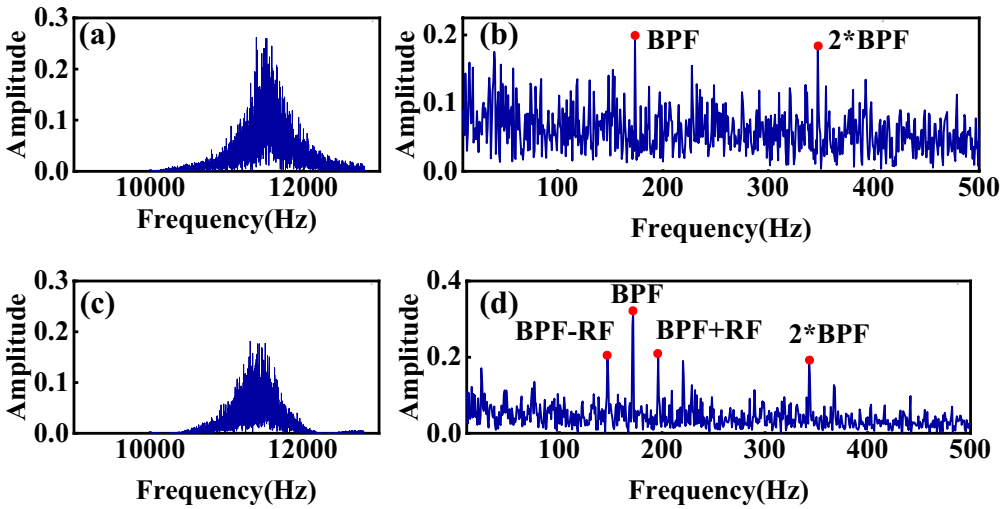

Figure 13 Frequency spectrum and envelope spectrum of effective submode: **a** and **b** for – 20 dB, **c** and **d** for – 10 dB

value mainly encompasses the CCFs and their harmonics, from which we can easily determine the target mode for further envelope analysis. Moreover, we found that the higher-frequency broadbands over 10 kHz carried more modulated information, as the BPF can be observed in Figure 11(a), (b) and Figure 12. Combined with the fact that more energy is concentrated in the band illustrated in Figure 10(c), it is reasonable to regard the submode with the highest frequency band as the main cavitation-induced vibration signal during 0–12.8 kHz.

6 Conclusions

This study proposed a novel SVMD that operates with a recursive framework and an improved HOSSA optimization process for cavitation diagnostics in fluid machinery, with a special focus on low-SNR conditions. Two objective functions were constructed by integrating the kurtosis and entropy index, referred to as KSE and ESK. Two steps were implemented to narrow the original α space to reduce computational burden. The following conclusions were drawn:

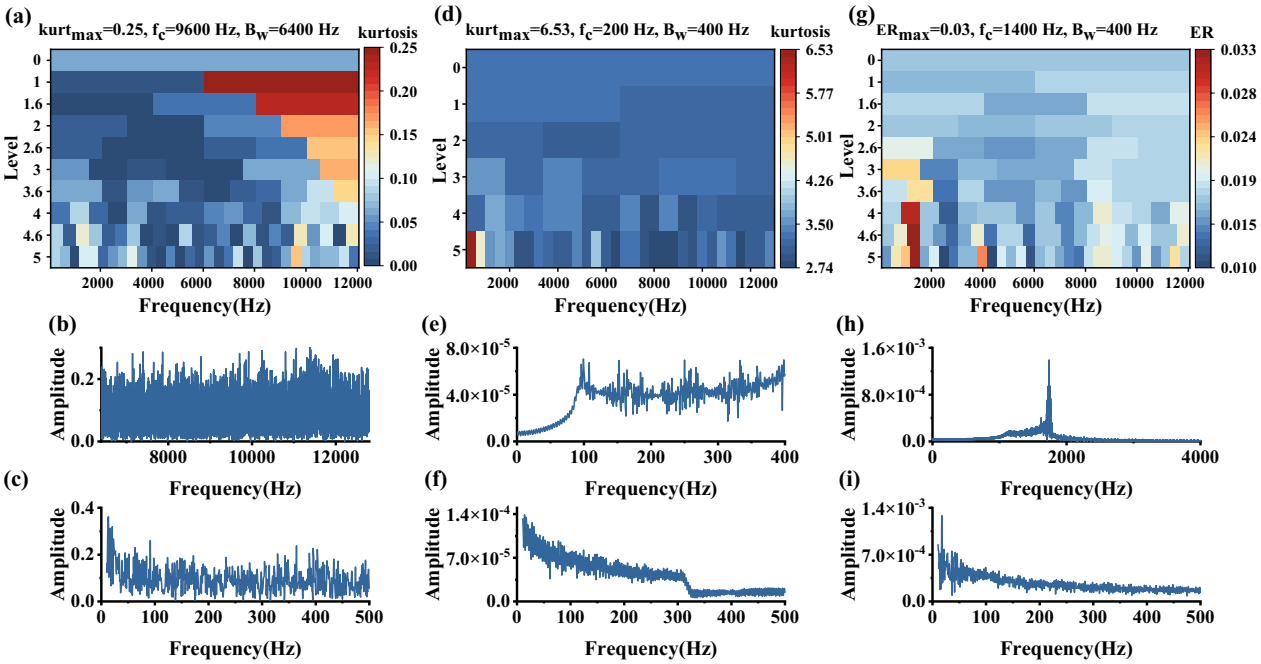

Figure 14 Diagnosis results of pump cavitation-induced signals under – 20 dB SNR conditions: **a**, **b**, and **c** for Kurtogram, **d**, **e**, and **f** for Autogram, and **g**, **h**, and **i** for IESCFFOgram

(1) The proposed SVMD can adaptively determine the decomposed number K and penalty factor α without any prior knowledge of the pending signals. Benefiting from the personalized α for each submode, the availability of SVMD is guaranteed to improve the signal decomposition performance under strong interference.
(2) Comparisons with parameter-optimized VMD, CEEMD, and SK demonstrate that SVMD almost achieves the best decomposition results among the VMD-based methods in the simulation datasets of noiseless and noisy signals. The decomposition accuracy for harmonic signals and impact signals can still reach 63.14% and 72.02%, respectively, under a – 10 dB environment.
(3) Benefiting from the reduced optimization space and faster convergence speed of the developed HOSSA itself, SVMD provides 4.7–14.2 times higher decomposition efficiency than other parameter-optimized VMDs.
(4) The submode corresponding to the highest EK value is the target mode containing CCFs. The comparison demonstrates the capability of SVMD in detecting whether cavitation occurs based on the identification of the blade passing frequency and its harmonics, even under a – 20 dB environment, which could potentially provide an alternative for the condition monitoring and fault diagnosis of fluid machinery.
(5) Further systemic studies are required to evaluate the effects of α markers and the reference mode on the decomposition results. The application of SVMD in hydro turbines will be the subject of our subsequent work.

Acknowledgements
Not applicable.

Authors' Contributions
HL was in charge of the investigation, methodology, experiment and was a major contributor in writing the manuscript. BS was in charge of experiments. ZT and ST were responsible for conceptualization and provided guidance on the experiment design and data analysis methods. All authors read and approved the final manuscript.

Author's Information
Hao Liu born in 1996, is currently a PhD candidate at *State Key Laboratory of Fluid Power and Mechatronic Systems, Zhejiang University, China*. His research interests include fault diagnostics and digital design of fluid machinery.
Zheming Tong born in 1988, is currently a professor at *State Key Laboratory of Fluid Power and Mechatronic Systems, Zhejiang University, China*. His research focuses on rotating machinery design.
Bingyang Shang born in 1998, is currently a PhD candidate at *State Key Laboratory of Fluid Power and Mechatronic Systems, Zhejiang University, China*. His research interests include pump design.
Shuiguang Tong born in 1960, is currently a professor at *State Key Laboratory of Fluid Power and Mechatronic Systems, Zhejiang University, China*. His research interests include lightweight design, industry-scale boiler design and inverse engineering.

Funding
Supported by National Natural Science Foundation of China (Grant No.52075481), Zhejiang Provincial Natural Science Foundation of China (Grant No. LD21E050003) and Central Government Fund for Regional Science and Technology Development of China (Grant No. 2023ZY1033).

Data availability
Data will be made available on request.

Declarations

Competing Interests
The authors declare no competing financial interests.

Received: 24 November 2022 Revised: 10 July 2023 Accepted: 21 July 2023
Published online: 07 September 2023

References

[1] X Luo, B Ji, Y Tsujimoto. A review of cavitation in hydraulic machinery. *Journal of Hydrodynamics*, 2016, 28: 335-58.
[2] Z Tong, H Liu, X E Cao, et al. Cavitation diagnosis for water distribution pumps: An early-stage approach combing vibration signal-based neural network with high-speed photography. *Sustainable Energy Technologies and Assessments*, 2023, 55: 102919.
[3] D Wu, Y Ren, J Mou, et al. Unsteady flow and structural behaviors of centrifugal pump under cavitation conditions. *Chinese Journal of Mechanical Engineering*, 2019, 32: 1-15.
[4] J Pei, W Wang, S Yuan, et al. Optimization on the impeller of a low-specific-speed centrifugal pump for hydraulic performance improvement. *Chinese Journal of Mechanical Engineering*, 2016, 29: 992-1002.
[5] D Li, R Gong, H Wang, et al. Entropy production analysis for hump characteristics of a pump turbine model. *Chinese Journal of Mechanical Engineering*, 2016, 29: 803–812.
[6] Z Tong, Z Yang, S Tong, et al. Investigating the hydraulic performance of slanted axial flow pumps using an enstrophy dissipation-based hybrid optimization approach. *Physics of Fluids*, 2022, 35(5).
[7] Z Zhou, Q Zheng, C Ding, et al. Effect of surface burnishing process with different strain paths on the copper microstructure. *Journal of Manufacturing Processes*, 2021, 71: 653-68.
[8] J Xin, Z Tong, W Zhu, et al. A patch-based flow field reconstruction method for particle image velocimetry data of multistage centrifugal pumps. *Journal of Fluids Engineering*, 2022, 144(12): 121502.
[9] J Antoni. Cyclic spectral analysis in practice. *Mechanical Systems and Signal Processing*, 2007, 21: 597-630.
[10] S Li, N Chu, P Yan, et al. Cyclostationary approach to detect flow-induced effects on vibration signals from centrifugal pumps. *Mechanical Systems and Signal Processing*, 2019, 114: 275-89.
[11] Y Wang, F Zhang, S Yuan, et al. Influence of cavitation on unsteady vortical flows in a side channel pump. *Chinese Journal of Mechanical Engineering*, 2023, 36(1): 25.
[12] G Mousmoulis, C Yiakopoulos, G Aggidis, et al. Application of spectral kurtosis on vibration signals for the detection of cavitation in centrifugal pumps. *Applied Acoustics*, 2021, 182: 108289.
[13] J H Lee, J S Seo. Application of spectral kurtosis to the detection of tip vortex cavitation noise in marine propeller. *Mechanical Systems and Signal Processing*, 2013, 40: 222–236.
[14] H S Han, C N Lee, S H Jeon, et al. Development of an evaluation method to determine cavitation inception speed with aft hull vibration using kurtosis of the DEMON spectrum. *Ocean Engineering*, 2018, 152: 167-80.
[15] N Chu, L Wang, L Yu, et al. An adaptive autogram approach based on a CFAR detector for incipient cavitation detection. *Sensors*, 2020, 20: 2303.
[16] K Wu, N Chu, D Wu, et al. The Enkurgram: A characteristic frequency extraction method for fluid machinery based on multi-band demodulation strategy. *Mechanical Systems and Signal Processing*, 2021, 155: 107564.
[17] K Wu, Y Xing, N Chu, et al. A carrier wave extraction method for cavitation characterization based on time synchronous average and time-frequency analysis. *Journal of Sound and Vibration*, 2020, 489: 115682.
[18] F Bao, X Wang, Z Tao, et al. EMD-based extraction of modulated cavitation noise. *Mechanical Systems and Signal Processing*, 2010, 24: 2124-36.
[19] R Azizi, B Attaran, A Hajnayeb, et al. Improving accuracy of cavitation severity detection in centrifugal pumps using a hybrid feature selection technique. *Measurement*, 2017, 108: 9-17.
[20] C Dai, S Hu, Y Zhang, et al. Cavitation state identification of centrifugal pump based on CEEMD-DRSN. *Nuclear Engineering and Technology*, 2023, 55: 1507-17.
[21] R Huang, R Qiu, Y Wang, et al. Space-time frequency spectra analyses of the unsteady cavitating vortical flows inside a mixed-flow pump. *Ocean Engineering*, 2021, 238: 109758.
[22] K Dragomiretskiy, D Zosso. Variational mode decomposition. *IEEE Transactions on Signal Processing*, 2013, 62: 531-44.
[23] X Jiang, J Wang, J Shi, et al. A coarse-to-fine decomposing strategy of VMD for extraction of weak repetitive transients in fault diagnosis of rotating machines. *Mechanical Systems and Signal Processing*, 2019, 116: 668-92.
[24] J Lian, Z Liu, H Wang, et al. Adaptive variational mode decomposition method for signal processing based on mode characteristic. *Mechanical Systems and Signal Processing*, 2018, 107: 53-77.
[25] M Zhang, Z Jiang, K Feng. Research on variational mode decomposition in rolling bearings fault diagnosis of the multistage centrifugal pump. *Mechanical Systems and Signal Processing*, 2017, 93: 460-93.
[26] A Kumar, C Gandhi, Y Zhou, et al. Variational mode decomposition based symmetric single valued neutrosophic cross entropy measure for the identification of bearing defects in a centrifugal pump. *Applied Acoustics*, 2020, 165: 107294.
[27] Z Wang, W Du, J Wang, et al. Research and application of improved adaptive MOMEDA fault diagnosis method. *Measurement*, 2019, 140: 63-75.
[28] X Yan, M Jia, L Xiang. Compound fault diagnosis of rotating machinery based on OVMD and a 1.5-dimension envelope spectrum. *Measurement Science and Technology*, 2016, 27: 075002.
[29] X Zhang, Q Miao, H Zhang, et al. A parameter-adaptive VMD method based on grasshopper optimization algorithm to analyze vibration signals from rotating machinery. *Mechanical Systems and Signal Processing*, 2018, 108: 58-72.
[30] Y Miao, M Zhao, J Lin. Identification of mechanical compound-fault based on the improved parameter-adaptive variational mode decomposition. *ISA Transactions*, 2019, 84: 82–95.
[31] C Yi, Y Lv, Z Dang. A fault diagnosis scheme for rolling bearing based on particle swarm optimization in variational mode decomposition. *Shock and Vibration*, 2016, 2: 1-10.
[32] X Yan, M Jia. Application of CSA-VMD and optimal scale morphological slice bispectrum in enhancing outer race fault detection of rolling element bearings. *Mechanical Systems and Signal Processing*, 2019, 122: 56-86.
[33] J Gai, J Shen, Y Hu, et al. An integrated method based on hybrid grey wolf optimizer improved variational mode decomposition and deep neural network for fault diagnosis of rolling bearing. *Measurement*, 2020, 162: 107901.
[34] J Xue, B Shen. A novel swarm intelligence optimization approach: Sparrow search algorithm. *Systems Science & Control Engineering*, 2020, 8: 22-34.
[35] T Barszcz, A Jabłoński. A novel method for the optimal band selection for vibration signal demodulation and comparison with the Kurtogram. *Mechanical Systems and Signal Processing*, 2011, 25: 431-51.
[36] D Wang, W T Peter, K L Tsui. An enhanced Kurtogram method for fault diagnosis of rolling element bearings. *Mechanical Systems and Signal Processing*, 2013, 35: 176-99.
[37] H Zhang, X Chen, Z Du, et al. Kurtosis based weighted sparse model with convex optimization technique for bearing fault diagnosis. *Mechanical Systems and Signal Processing*, 2016, 80: 349-76.
[38] Y Lei, J Lin, Z He, et al. Application of an improved kurtogram method for fault diagnosis of rolling element bearings. *Mechanical Systems and Signal Processing*, 2011, 25: 1738-49.
[39] Y Cheng, S Wang, B Chen, et al. An improved envelope spectrum via candidate fault frequency optimization-gram for bearing fault diagnosis. *Journal of Sound and Vibration*, 2022, 523: 116746.